Journal of Solid State Chemistry 183 (2010) 761–768

Contents lists available at ScienceDirect

Journal of Solid State Chemistry

journal homepage: www.elsevier.com/locate/jssc

Probing the local structure of crystalline ZITO: $In_{2-2x}Sn_xZn_xO_3$ ($x \leq 0.4$)

Cathleen A. Hoel [a], Jean-François Gaillard [b], Kenneth R. Poeppelmeier [a,*]

[a] Department of Chemistry, Northwestern University, 2145 Sheridan Road, Evanston, IL 60208, USA
[b] Department of Civil and Environmental Engineering, Northwestern University, 2145 Sheridan Road, Evanston, IL 60208, USA

ARTICLE INFO

Article history:
Received 18 October 2009
Received in revised form
14 January 2010
Accepted 18 January 2010
Available online 25 January 2010

Keywords:
Indium oxide
Cosubstitution
Solid solution
EXAFS
Transparent conducting oxide
X-ray absorption spectroscopy

ABSTRACT

The local structure of In_2O_3 cosubstituted with Zn and Sn ($In_{2-2x}Sn_xZn_xO_3$, $x \leq 0.4$ or ZITO) was determined by extended X-ray absorption fine structure (EXAFS) for x=0.1, 0.2, 0.3 and 0.4. The host bixbyite In_2O_3 structure is maintained up to the enhanced substitution limit (x=0.4). The EXAFS spectra are consistent with random substitution of In by the smaller Zn and Sn cations, a result that is consistent with the "good-to-excellent" conductivities reported for ZITO.

1. Introduction

Transparent conducting oxides (TCOs) exhibit both high electrical conductivity and optical transparency in the visible range, which makes them critical materials for flat-panel displays, LEDs, photovoltaics and energy-efficient windows [1,2]. The most commonly used TCO in high-end electronics is $In_{2-x}Sn_xO_{3-\delta}$ ($x \approx 0.1$, ITO) owing to its high conductivity of 10^3–10^4 S/cm and 90% visible transparency as a thin film when ~400 nm thick [3,4]. The natural scarcity of indium, however, has motivated the search for indium-free TCOs.

In 1997 Palmer et al. [5] discovered the transparent conductor Zn and Sn cosubstituted In_2O_3 (ZITO), where the cosubstitution of Zn^{2+}/Sn^{4+} pairs for two In^{3+} atoms can displace up to 40% of the indium, which gives the general formula $In_{2-2x}Sn_xZn_xO_3$ ($x \leq 0.4$). The conductivity of bulk ZITO for specimens with strict equivalents of Zn and Sn ([Sn]=[Zn]) increases from 400 to 600 S/cm as x increases from 0.05 to 0.4. When ZITO is prepared with a slight Sn excess ([Sn] > [Zn]), the conductivity for x=0.05 is 2500 S/cm, which nears that of an ITO control (5% Sn, cation basis) with 2700 S/cm. The conductivity of ZITO then decreases to 600 S/cm for a Sn-excess specimen at x=0.4 [5,6]. Therefore, while the optimal conductivity of ZITO does not surpass that of ITO, ZITO offers an option to significantly lower the concentration of In without a large decrease in conductivity. This work will examine the average coordination environment of each element in the solid solution $In_{2-2x}Sn_xZn_xO_3$ ($x \leq 0.4$) with extended X-ray absorption spectroscopy.

2. Structure of In_2O_3 and ZITO

Bixbyite In_2O_3 can be described as a fluorite-type structure with one quarter of the anions missing. In the fluorite structure, the cations reside at the body center of a cube of eight anions. In the bixbyite structure two anions are missing from each cube, either across a body diagonal (b site) or a face diagonal (d site) as shown in Fig. 1. The anions are distorted from the ideal cubic vertices, which cause the b site to have six equivalent In–O bonds and the d site to have three pairs of equivalent In–O bonds. The space group of In_2O_3 is *Ia-3* (no. 206) with the lattice constant a=10.117 Å [7]. In an ideal cosubstitution, the Zn and Sn replace the In with no site preference giving a statistically homogeneous distribution of cations throughout the oxide matrix.

3. Experimental

3.1. Synthesis of ZITO

Four different compositions of ZITO were prepared by solid-state reactions: $In_{1.8}Sn_{0.1}Zn_{0.1}O_3$ (ZITO-10), $In_{1.6}Sn_{0.2}Zn_{0.2}O_3$ (ZITO-20), $In_{1.4}Sn_{0.3}Zn_{0.3}O_3$ (ZITO-30) and $In_{1.2}Sn_{0.4}Zn_{0.4}O_3$ (ZITO-40). Stoichiometric amounts of the starting oxides, In_2O_3 (Alfa Aesar

* Corresponding author. Fax: +1 847 491 7713.
E-mail addresses: jf-gaillard@northwestern.edu (J.-F. Gaillard), krp@northwestern.edu (K.R. Poeppelmeier).

0022-4596/$ - see front matter © 2010 Elsevier Inc. All rights reserved.
doi:10.1016/j.jssc.2010.01.014

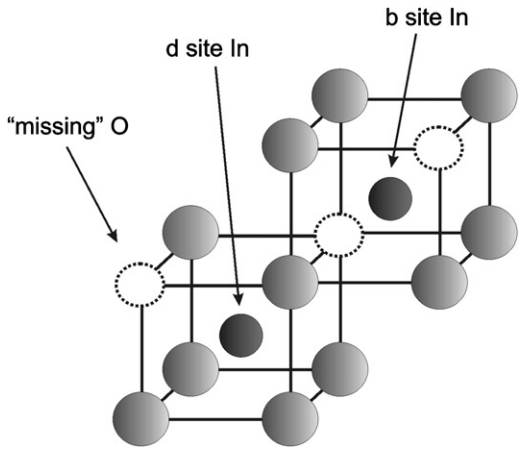

Fig. 1. A cartoon representing the two In environments in bixbyite In_2O_3. The dark grey spheres represent In, the light grey spheres represent O and the dashed circles represent the one-quarter anions missing from the fluorite structure. The O atoms are drawn in the idealized fluorite positions—the actual bixbyite O positions are distorted off the cube vertices.

99.99%), SnO_2 (Aldrich, 99.9%) and ZnO (Sigma-Aldrich, 99.99%) were ground together under acetone in an agate mortar and pestle. Approximately 0.75 g of the mixed powder was pressed into a pellet of 13 mm in diameter. The pellet was placed in an alumina crucible surrounded by sacrificial powder of the same composition. The crucible was capped with a lid and set inside another capped alumina crucible, which was placed inside a third capped alumina crucible. These multiple alumina containers were found necessary to prevent Zn vaporization and ensure [Sn]=[Zn] for each x [5,8]. The sample inside the set of three crucibles was heated for 24 h at 1100 °C then ground to a powder, repressed into a pellet and heated for 24 h at 1250 °C. These pellets, which were a green color, were ground into a powder for X-ray diffraction and absorption measurements.

3.2. X-ray diffraction

Powder X-ray diffraction (XRD) was measured using a Rigaku (Tokyo, Japan) diffractometer (40 kV, 20 mA) with Ni-filtered Cu Kα radiation. Scans were measured over the range 2θ=20–70° with a 0.05° step size and 1 s dwell time. The measured patterns were corrected for detector drifting with an external Si standard (640c, NIST) and analyzed with the software JADE 5.0 (Materials Data Inc., Livermore, CA).

3.3. X-ray absorption spectroscopy

The ZITO samples and In_2O_3, SnO_2 and ZnO standards were prepared for EXAFS measurements by spreading a uniform layer of the powder onto low-absorbing adhesive Scotch™ tape [9] and adjusting the number of stacked layers to obtain $\mu \approx 2$ and $\Delta\mu(E_0) \approx 1$. A typical EXAFS measurement at the In K edge required 8 layers of tape, whereas measurements at the Zn and Sn K edge required 16 layers. All measurements were performed at room temperature.

The X-ray absorption spectra were measured at the Argonne National Laboratory Advanced Photon Source (ANL-APS) beamline operating at 100 mA and 7.0 GeV. The double-crystal monochromator consisted of parallel Si(1 1 1) crystals, which were detuned to 70% of the maximum beam intensity to reject higher order harmonics. Each measurement included an In, Sn or Zn metal foil reference to calibrate the absorption edge energy. The edge energy was chosen at the inflection point—where the second derivative equals zero. The edge energies were set at 27940 eV for In, 29200 eV for Sn and 9659 eV for Zn. Both the standards and the samples were measured in transmission mode using Oxford ionization chambers with a path length of 30 cm. The chambers were filled with gas mixtures of He, N_2 and Ar to obtain 10% absorption for the incident beam, I_0, 20% absorption for the sample transmitted beam, I_T, and 60% absorption for the reference foil transmitted beam, I_{T2}. The Sn and Zn measurements were replicated 5 times to increase the signal-to-noise ratio. ZITO-10 was measured at the In K edge only; the Sn and Zn concentrations were too low to obtain enough absorption for transmission measurements at the Sn and Zn K edges.

Background removal was performed using the AutoBK algorithm [10,11] as implemented in Athena [12], a graphical front-end for the IFFEFIT [12–14] software package. The data were normalized to an edge step height of one. The first inflection point of the absorption edge defined the edge energy, E_0, which was used to determine the photoelectron wave number: $k=\sqrt{2m_e(E-E_0)/\hbar}$ where m_e is the electron mass, $\hbar$ is Planck's constant, and E is the incident X-ray energy. Both the samples and standards were measured from 250 eV below the edge to 1230 eV above the In and Sn K edge (k=18 Å^{-1}). The samples and standards were measured from 150 eV below the edge to 1230 eV above the Zn K edge. The $\chi(k)$ spectra was Fourier transformed with a sine window over the region k=3.3–13.0 Å^{-1} for the In data, k=2.4–11.3 Å^{-1} for the Sn data and k=2.4–10.7 Å^{-1} for the Zn data to obtain the radial structure function (RSF). Modeling and simulations of the EXAFS spectra were performed using the FEFF 6.0 code [15] as implemented in Artemis [12]. The goodness-of-fit was determined by minimizing the residual component, $R=\sum_i(\text{data}_i-\text{fit}_i)^2/\sum_i\text{data}_i^2$, between the model and experimental values [16]. The model was fit in real space over the ranges R=1.0–5.4 Å for the In and Sn data while R=1.0–4.0 Å for the Zn data. All the Fourier transforms shown are uncorrected for phase shifts.

4. Results and discussion

4.1. X-ray diffraction

The XRD patterns for each ZITO composition exhibit only the peaks expected for the bixbyite In_2O_3 structure, which confirms the ZITO is single phase (Fig. 2). As the concentration of Zn and Sn

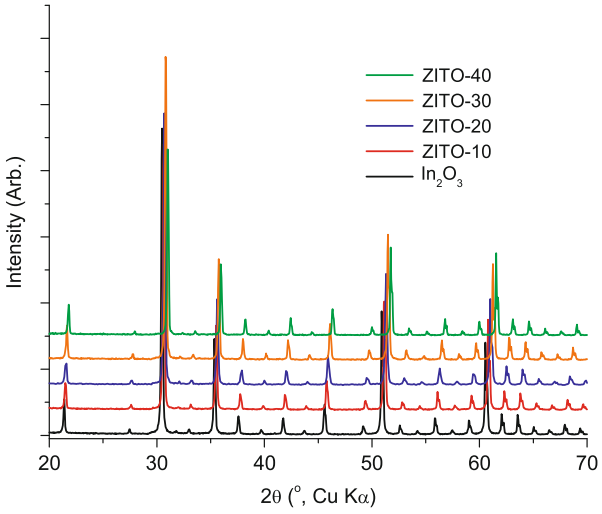

Fig. 2. (Color online) XRD patterns of ZITO at each x compared to In_2O_3. The peak shift to higher 2θ at higher Zn/Sn substitution levels indicates a lattice contraction.

increases, the peaks shift to higher 2θ positions. This shift indicates a contraction in the unit cell size, caused by the smaller radii of Sn^{4+} and Zn^{2+} (0.69 and 0.74 Å, respectively) compared to In^{3+} (0.79 Å) [17]. The lattice parameters, listed in Table 1, decrease linearly with respect to the cation percentage of In in accordance with Vegard's rule [18]. As shown on these X-ray diffraction results, Zn/Sn pairs randomly substitute for In without forming additional phases. Powder X-ray diffraction, however, only detects long-range order. X-ray absorption spectroscopy can be used to observe the local coordination environment.

Table 1
The lattice parameter, *a*, of each composition of ZITO and In_2O_3 determined from the XRD pattern.

	% In	*a* (Å)
In_2O_3	100	10.118(1)
ZITO-10	90	10.079(1)
ZITO-20	80	10.047(1)
ZITO-30	70	10.015(1)
ZITO-40	60	9.982(1)

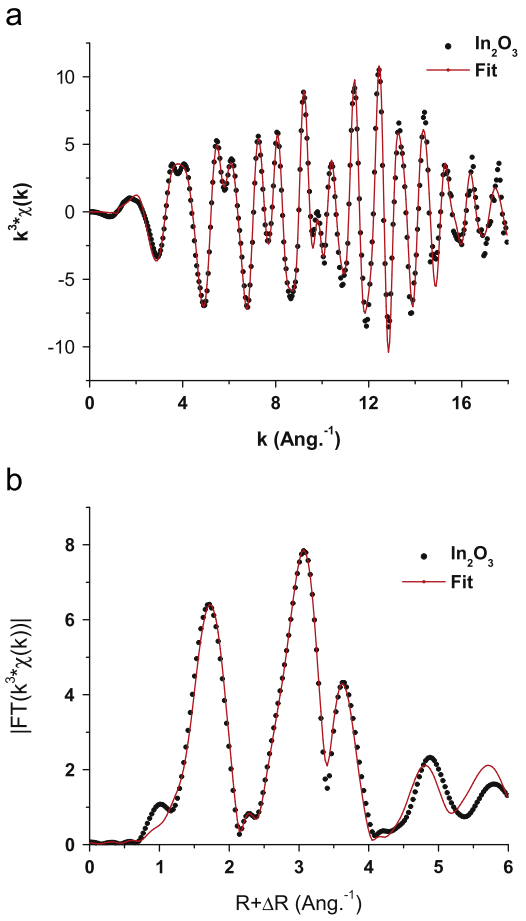

Fig. 3. (Color online) The best fit of In_2O_3 (line) overlaid the experimental spectrum (black dots) at the In K edge plotted as (a) $k^3 \cdot \chi(k)$ and (b) the k^3-weighted RSF.

4.2. Extended X-ray absorption fine structure

X-ray absorption spectroscopy is sensitive to the local structure and can elucidate the fine details of Zn and Sn substituted In_2O_3. Because EXAFS is element selective, the local structure around In, Sn and Zn can be examined separately for each individual ZITO sample. The passive electron reduction factor, S_0^2, was determined to be 1.0 for each element obtained from the best fit of a reference compound with a known crystallographic structure. The chosen references were bixbyite In_2O_3 [7], rutile SnO_2 [19] and wurtzite ZnO [20]. For each reference oxide, the coordination numbers were constrained to those of the ideal crystal structure, while the S_0^2 term was allowed to vary. Each model was separately fit to spectra with *k*-, k^2- and k^3-weighted data. The variations of the best fit values for the S_0^2 term at the various *k*-weighted spectra ranged from 1.0 to 1.1 ± 0.1. When S_0^2 was constrained to 1.0, the EXAFS interatomic distances match those of the crystallographic structure (see Fig. 3 and Table 1 for In_2O_3, Fig. S1 and Table S1 for SnO_2, and Fig. S2 and Table S2 for ZnO). All of the models discussed in this paper were constrained S_0^2=1.0.

Owing to thermal vibrations and the relative displacements of an atom from its ideal position, each neighbor is modeled with a Gaussian distribution factor, $e^{-2\sigma^2 k^2}$, where the variance, σ^2, is referred to as the mean square relative displacement (MSRD). The measurements presented throughout this paper were all taken at room temperature, so the MSRD cannot be separated to the thermal vibration term, $\sigma_{th}{}^2$, and positional displacement term, $\sigma_{displ}{}^2$. The EXAFS measurements were all taken at the same temperature, however, so the thermal vibration term will not vary between individual samples. The degree of the relative displacement of the neighbor position will dominate the variations of σ^2 as a function of *x* along the solid solution.

4.2.1. In K edge

The $k^3 \cdot \chi(k)$ and RSF for the experimental spectrum and best fit of the In_2O_3 standard are shown in Fig. 3 with the best fit results of the EXAFS model listed in Table 2. The In local structure was simulated with both the b and d sites, which consists of more than one neighbor distance per shell. For example, the first In–O shell of the b site has one bond length at 2.18 Å while the d site has three bond lengths at 2.12, 2.18 and 2.20 Å. The relative differences between the neighbor distances for a single shell were retained. For simplicity, the weighted average of each neighbor distance is reported. The first In–O shell was fit with six O at an average distance of 2.179 Å, which matches the crystallographic bond length of 2.18 Å. The second, third and fourth shells were each fit with six In–In shells at the average distances 3.357, 3.830 and 5.082 Å, which agree with the crystallographic values of 3.36, 3.83 and 5.08 Å.

Table 2
The values for the best fit to the In_2O_3 spectrum compared to the crystallographic values.

Neighbor	EXAFS neighbor distance (Å)	Crystal neighbor distance (Å)	EXAFS coord. number	Crystal coord. number	σ^2 (Å^2)	ΔE_0 (eV)
O	2.179(3)	2.18	**6**	6	0.0047(7)	5.6(5)
In	3.357(4)	3.36	**6**	6	0.0045(4)	2.1(6)
In	3.830(5)	3.83	**6**	6	0.0063(6)	2.1(6)
In	5.082(6)	5.08	**6**	6	0.0052(9)	6(1)

The goodness-of-fit for this model is *R*=0.011. The coordination numbers were constrained to the crystallographic values, as indicated by the bold font. The second and third shell ΔE_0 values were constrained to the same value.

The $\mu(E)$, $k^3 \cdot \chi(k)$ and respective RSFs of In_2O_3, ZITO-10, -20, -30 and -40 are plotted in Fig. 4. The $\mu(E)$ and $k^3 \cdot \chi(k)$ spectra of ZITO exhibit the same resonances as the In_2O_3 standard, which indicates ZITO has the same structural features as In_2O_3. The noted difference between each of the spectra is the decrease of amplitude associated with an increase of x. The same amplitude reduction occurs in the RSF for the peaks located at $R > 2.5$ Å. Of the RSF spectra shown, In_2O_3 has the strongest peak intensities at $R > 2.5$ Å while ZITO-40 has the weakest peak intensities.

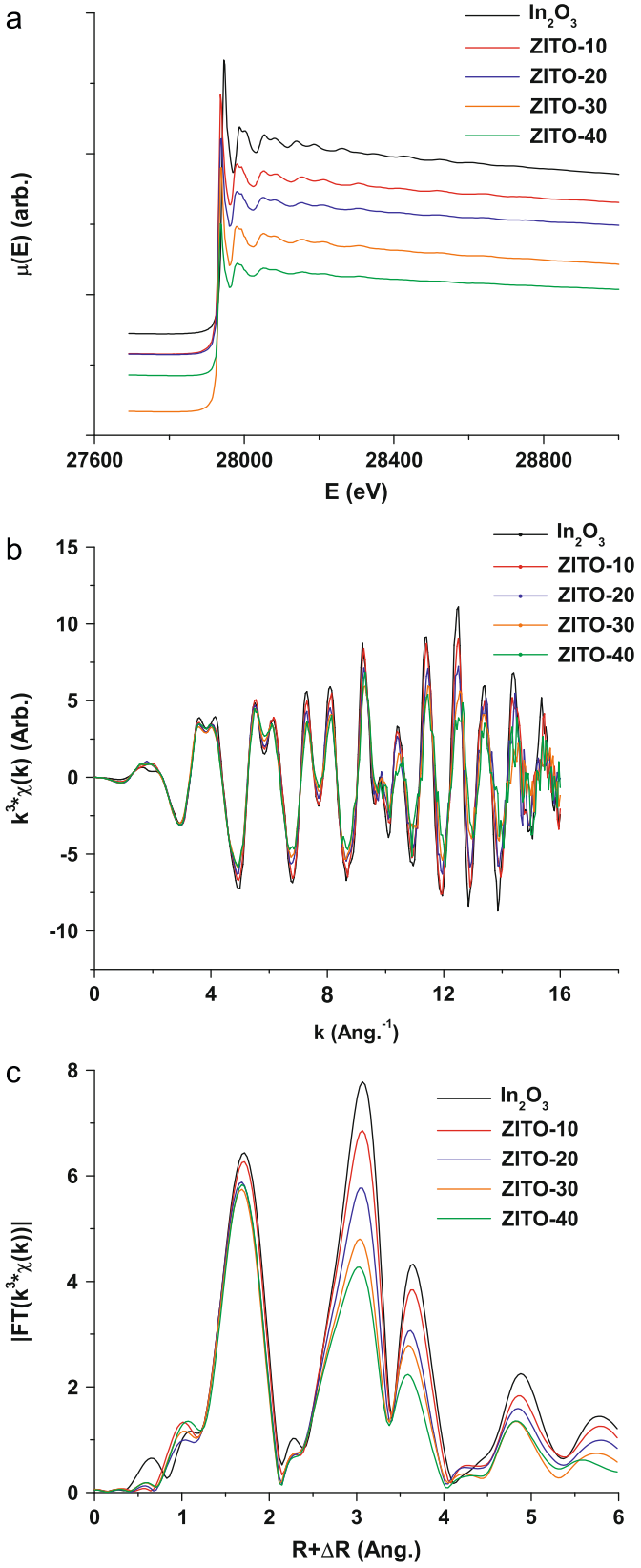

Fig. 4. (Color online) The experimental EXAFS spectra of In_2O_3 and ZITO at the In K edge plotted as (a) $\mu(E)$, (b) k^3 $\chi(k)$ and (c) the k^3-weighted RSF.

The substitution of In by Zn and Sn alter the total X-ray absorption coefficient owing to their different scattering factors. The photoelectron waves, which were backscattered by In and Sn neighbors, constructively interfere owing to their adjacent atomic numbers of 49 and 50, respectively. Zn, however, has less electron density than In and Sn, which is characterized by a different phase shift and leads to destructive interference. This phenomenon is illustrated in Fig. 5, which shows the calculated photoelectron waves produced by a core electron ejected from an In absorber and single scattered by an In, Sn and Zn neighbor. The neighbor distance and MSRD were set at 3.34 Å and 0.005 $Å^2$, respectively, for all three cation scatterers. The In–Zn scattering wave is out of phase with the In–In and In–Sn photoelectron waves, resulting in the destructive interference of the overall EXAFS signal.

The EXAFS models of Zn and Sn cosubstituted In_2O_3 was generated from the In_2O_3 crystallographic positional coordinates with the adjusted lattice parameter and composition for each x. The RSFs were calculated for ZITO at each x with the same scattering paths and MSRDs as the best fit for In_2O_3 (Fig. 6). The regular decrease in the amplitude with increased Zn and Sn substitution is apparent, which mimics the experimental results. When a simulated spectrum is compared to an experimental spectrum for a given composition, the simulation tends to overestimate the observed amplitude of the RSF peaks. The additional attenuation in the experimental spectrum is likely caused by an increased MSRD.

The best fit values for the Zn and Sn-substituted In_2O_3 models are listed in Table 3. The EXAFS coordination numbers were set to the crystallographic coordination numbers with the ideal fractional site occupancy for each element. The bond length, MSRD and edge energy shift for each shell were allowed to vary. The first In–O shell for ZITO-10, -20, -30 and -40 was fit with six O at an average distance of 2.16 Å compared to the In_2O_3 In–O distance of 2.18 Å. The In–O bond length was unchanged within uncertainty as a function of x. The second, third and fourth shells

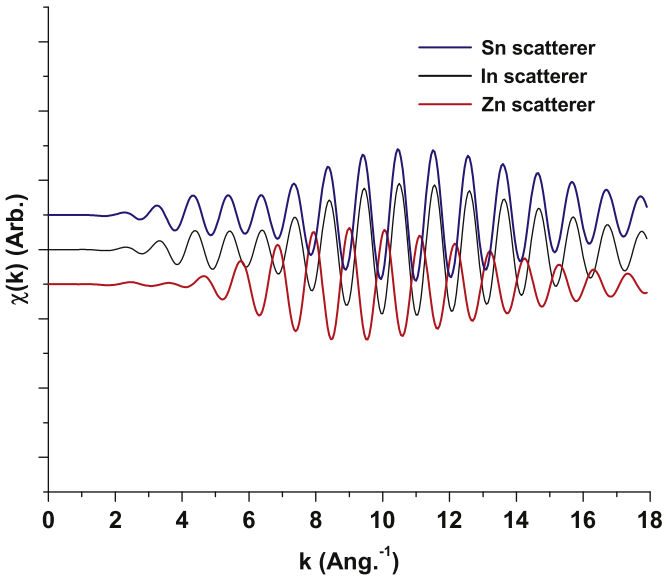

Fig. 5. (Color online) The photoelectron waves from an In absorber single scattered by an In, Sn and Zn neighbor. The photoelectron wave scattered from Zn destructively interferes with the photoelectron waves scattered from In and Sn.

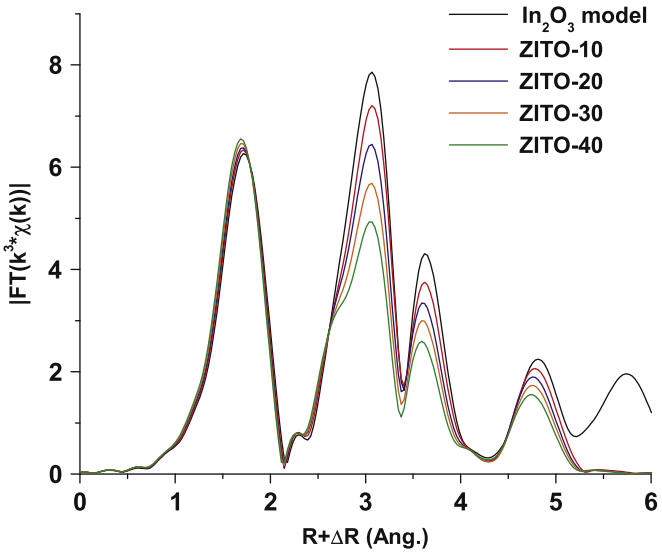

Fig. 6. (Color online) The calculated ZITO EXAFS spectra at the In K edge generated by stoichiometric substitution of Zn and Sn into the In_2O_3 model. The simulated spectra follow the same trend seen in the experimental spectra of decreasing amplitude with In concentration.

Table 3
The values for the best fits to the ZITO spectra at the In K edge.

In edge	Neighbor	Neighbor distance (Å)	C.N.	σ^2 (Å^2)	ΔE_0 (eV)	*R*-factor
ZITO-10	O	2.161(3)	**6**	0.0040(4)	4.4(9)	0.012
	In/Sn/Zn	3.348(5)	**6**	0.0042(3)	2.8(7)	
	In/Sn/Zn	3.820(5)	**6**	0.0060(6)	2.8(7)	
	In/Sn/Zn	5.068(7)	**6**	0.005(1)	6.8(1.5)	
ZITO-20	O	2.161(3)	**6**	0.0046(4)	3.8(8)	0.012
	In/Sn/Zn	3.340(5)	**6**	0.0045(3)	1.3(7)	
	In/Sn/Zn	3.810(5)	**6**	0.0067(6)	1.3(7)	
	In/Sn/Zn	5.056(8)	**6**	0.005(1)	6(2)	
ZITO-30	O	2.157(4)	**6**	0.0049(4)	3.1(8)	0.012
	In/Sn/Zn	3.328(5)	**6**	0.0048(3)	0.2(8)	
	In/Sn/Zn	3.797(6)	**6**	0.0065(6)	0.2(8)	
	In/Sn/Zn	5.038(8)	**6**	0.006(1)	6(2)	
ZITO-40	O	2.162(4)	**6**	0.0048(4)	3.8(9)	0.016
	In/Sn/Zn	3.321(7)	**6**	0.0047(4)	0(1)	
	In/Sn/Zn	3.789(8)	**6**	0.0072(9)	0(1)	
	In/Sn/Zn	5.027(10)	**6**	0.005(2)	6(2)	

The coordination numbers were constrained to the crystallographic values, as indicated by the bold font. The second and third shell ΔE_0 were constrained to the same value.

were fit with six In–M neighbors, such that M represents the fractional occupancy of In, Sn and Zn for each *x* along the solid solution. The second, third and fourth shell distances each contracted with higher values of *x*. ZITO-10 was fit with six neighbors (90% In, 5% Sn, 5% Zn) at an average distance of 3.357 Å, while ZITO-40 was fit with six neighbors (60% In, 20% Sn, 20% Zn) at 3.321 Å for ZITO-40. The third and fourth shells each have six neighbors at 3.820 and 5.080 Å for ZITO-10, which shorten to 3.789 and 5.027 Å for ZITO-40.

The first In–O bond shortens when Zn and Sn substitute for In from 2.18 Å for In_2O_3 to 2.16 Å for ZITO-10. The In–O bond length, however, does not continue to contract as more Zn and Sn substitute for In. If the In–O bond distance decreased with respect to the unit cell size, the average distance for ZITO-10, -20, -30 and -40 would be 2.170, 2.163, 2.156 and 2.149 Å, respectively. Rather, the In–O distance stays at 2.16 Å for ZITO-40 because the large In^{3+} cation controls the size of this octahedral unit. The second, third and fourth shells, on the other hand, do exhibit shorter distances with higher Zn and Sn concentrations. This observation is expected because these shells include the smaller Zn^{2+} and Sn^{4+} cations, which are responsible for the net lattice contraction demonstrated by the XRD patterns. The higher values of *x* along the solid solution should exhibit shorter interatomic distances between the cations, which are consistent with the observations.

4.2.2. Sn K edge

The k^3-weighted RSFs of ZITO-20, -30 and -40 are plotted in Fig. 7. The ZITO spectra show the marked amplitude drop at higher values of *x* owing to the increased destructive interference between the Sn–In and Sn–Sn photoelectron waves and the Sn–Zn photoelectron waves. The local Sn environment was fit to the Zn and Sn-substituted In_2O_3 model. The model and experimental spectrum of ZITO-20 is plotted as the k^3-weighted RSF in Fig. 8 and the values for the best fit are listed in Table 4. The coordination numbers were constrained to the crystallographic values while the bond distances, MSRD and edge energy shift were allowed to vary

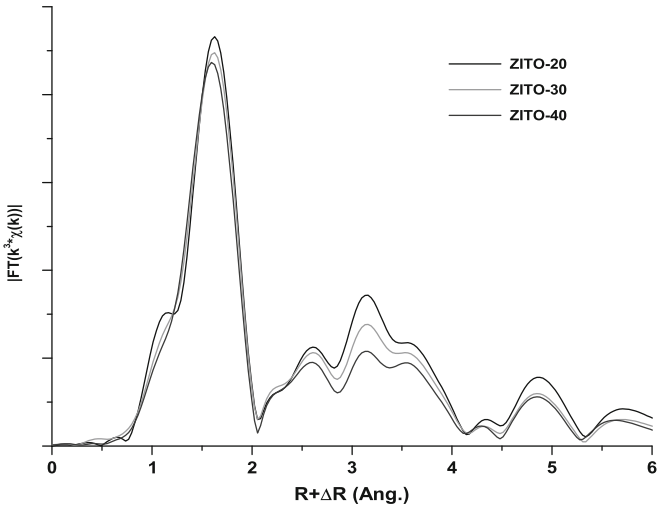

Fig. 7. (Color online) The experimental EXAFS spectra of ZITO-20, -30 and -40 at the Sn K edge plotted as the k^3-weighted RSF.

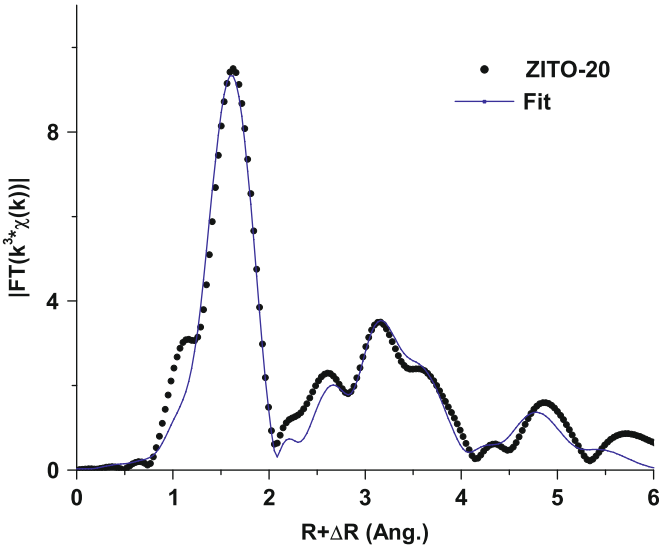

Fig. 8. (Color online) The best fit of ZITO-20 (line) overlay the experimental spectrum (black dots) at the Sn K edge plotted as the k^3-weighted RSF.

Table 4
The values for the best fits to the ZITO spectra at the Sn K edge.

Sn edge	Neighbor	Neighbor distance (Å)	C.N.	σ^2 (Å^2)	ΔE_0 (eV)	*R*-factor
ZITO-20	O	2.080(7)	**6**	0.0023(5)	6.3(9)	0.024
	In/Sn/Zn	3.357(13)	**6**	0.0046(8)	6.5(1.3)	
	In/Sn/Zn	3.827(13)	**6**	0.004(1)	6.5(1.3)	
	In/Sn/Zn	5.024(13)	**6**	0.005(3)	6.5(1.3)	
ZITO-30	O	2.079(6)	**6**	0.0025(5)	6.3(8)	0.018
	In/Sn/Zn	3.349(13)	**6**	0.0050(8)	6(1)	
	In/Sn/Zn	3.818(13)	**6**	0.004(1)	6(1)	
	In/Sn/Zn	5.005(13)	**6**	0.005(3)	6(1)	
ZITO-40	O	2.073(6)	**6**	0.0027(4)	5.7(7)	0.016
	In/Sn/Zn	3.339(13)	**6**	0.0052(9)	6(1)	
	In/Sn/Zn	3.805(13)	**6**	0.003(2)	6(1)	
	In/Sn/Zn	4.985(13)	**6**	0.005(3)	6(1)	

The coordination numbers were constrained to the crystallographic values, as indicated by the bold font. The second, third and fourth shell ΔE_0 were constrained to the same value.

for each shell. The $k^3 \cdot \chi(k)$ spectra and model of ZITO-20 are plotted in Figs. S3 and S4, respectively, in the supplementary information.

The first Sn–O shell was fit with six O at an average distance of 2.080 Å. This Sn–O bond length is much closer to that of SnO_2 at 2.05 Å compared to the In–O bond in In_2O_3 at 2.179 Å. This first shell Sn–O bond contraction was observed by several other teams for ITO [21–24]. The Sn–O bond decreases from 2.080 Å for ZITO-20 to 2.073 Å for ZITO-40. The second, third and fourth Sn–M shell neighbors were fit with six M neighbors each, where M is In, Sn and Zn weighted by its fractional occupancy. The neighbor distances for each shell contract along the solid solution with 3.357, 3.827 and 5.024 Å for ZITO-20, which decrease to 3.339, 3.805 and 4.985 Å for ZITO-40, respectively.

The Sn–O bond of 2.08 Å is significantly shorter than the In–O bond of 2.16 Å for ZITO, which is caused by the smaller size of Sn^{4+} compared to In^{3+}. These small Sn–O octahedral units shrink the unit cell, which manifests as the contracted Sn–M distances observed in the second, third and fourth shells. As more Zn and Sn are present in ZITO, the interatomic distances reduce further.

4.2.3. Zn K edge

The k^2-weighted RSFs of ZITO-20, -30, and -40 are plotted in Fig. 9. The ZITO spectra show the amplitude reduction, which corresponds to the decreased In content. The individual Zn–In and Zn–Sn scattering waves destructively interfere with the Zn–Zn photoelectron waves. The local Zn environment was fit to the Zn and Sn-substituted In_2O_3 model using a single Zn–O bond distance for the first shell. The model and experimental spectrum of ZITO-20 is plotted as the k^2-weighted RSF in Fig. 10 and the best fit values are listed in Table 5. The coordination numbers were set to the crystallographic values while the bond distance, MSRD and edge energy shift for each shell were allowed to vary. The $k^2 \cdot \chi(k)$ spectra and model of ZITO-20 are plotted in Figs. S5 and S6, respectively, in the supplementary information.

Because tetrahedral Zn–O is stable, the coordination number of the first oxide shell needed to be verified. Previous reports on the X-ray absorption near edge structure (XANES) of Zn^{2+} showed that materials with ZnO_6^{10-} octahedra exhibit stronger white lines than ZnO_4^{6-} tetrahedra. The XANES of ZITO-20 shows a stronger white line than that of ZnO (Fig. 11). Furthermore, the line shape of the ZITO-20 spectrum is characteristic of ZnO_6^{10-} octahedral units both seen experimentally and theoretically [25]. Therefore, the first Zn–O shell was fit with six O at a distance of 2.08 Å—the same length as the Sn–O bond for ZITO. The first shell contracts from 2.084 Å for ZITO-20 to 2.075 Å for ZITO-40. The second and third In–M shells

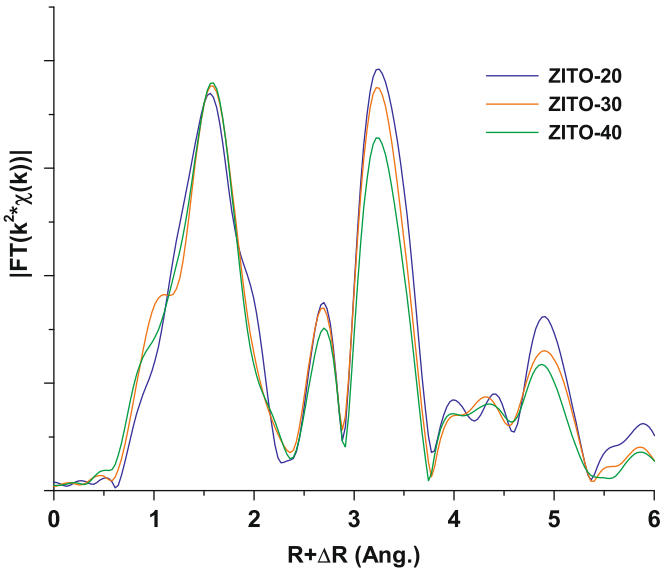

Fig. 9. (Color online) The experimental EXAFS spectra of ZITO-20, -30 and -40 at the Zn K edge plotted as the k^2-weighted RSF.

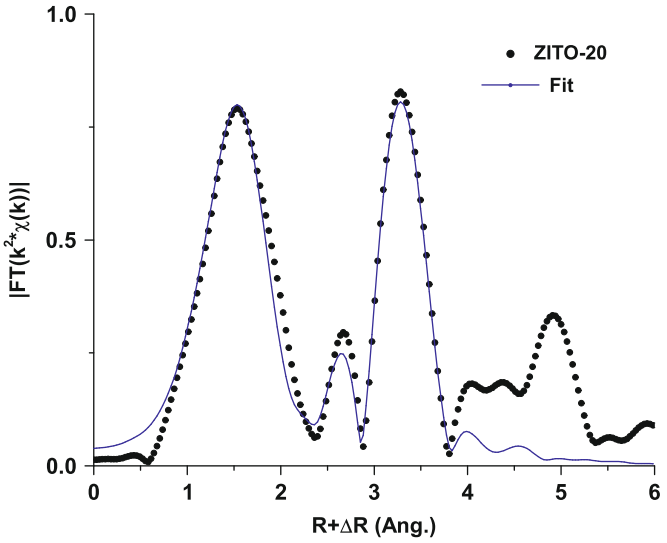

Fig. 10. (Color online) The best fit of ZITO-20 (line) overlay the experimental spectrum (black dots) at the Zn K edge plotted as the k^2-weighted RSF.

were fit with six M neighbors each, where M is the weighted composition of In, Sn and Zn. The average distances for the second and third shells were 3.293 and 3.745 Å for ZITO-20 and did not move outside of uncertainty for ZITO-30 or -40.

The short Zn–O bond arises from the small size of the Zn^{2+} cation. Although the octahedral Zn^{2+} radius at 0.74 Å is reported to be larger than the Sn^{4+} radius at 0.69 Å, the Zn–O and Sn–O bond lengths are both 2.08 Å. The Zn-cation distances do not contract with higher values of *x*. Instead, the second and third shell distances have large uncertainties and MSRDs, which suggests Zn resides off-center in the bixbyite b and d site octahedral units. Asymmetric six-coordinate Zn–O units have been observed for $ZnSO_4$ and ZnC_2O_4, which exhibit Zn–O distances ranging from 1.94 to 2.34 Å.

The EXAFS spectra of all three cations present RSF peak amplitude reduction with increased values of *x*. The amplitude reduction was attributed to the substitution of Zn on In sites, which added a destructive component to the EXAFS signal. This result

Table 5
The values for the best fits to the ZITO spectra at the Zn K edge.

Zn edge	Neighbor	Neighbor distance (Å)	C.N.	σ^2 (Å^2)	ΔE_0 (eV)	*R*-factor
ZITO-20	O	2.084(7)	**6**	0.016(1)	**0.5**	0.020
	In/Sn/Zn	3.293(13)	**6**	0.007(2)	1.8(9)	
	In/Sn/Zn	3.745(20)	**6**	0.008(2)	1.8(9)	
ZITO-30	O	2.080(6)	**6**	0.017(1)	**0.5**	0.017
	In/Sn/Zn	3.300(12)	**6**	0.008(1)	2.5(8)	
	In/Sn/Zn	3.748(22)	**6**	0.010(2)	2.5(8)	
ZITO-40	O	2.075(6)	**6**	0.017(1)	**0.5**	0.013
	In/Sn/Zn	3.294(12)	**6**	0.008(1)	2.6(8)	
	In/Sn/Zn	3.731(27)	**6**	0.009(2)	2.6(8)	

The coordination numbers were constrained to the crystallographic values and the first shell ΔE_0 were constrained to be the value 0.5 eV, as indicated by the bold font. The second and third shell ΔE_0 were constrained to the same value.

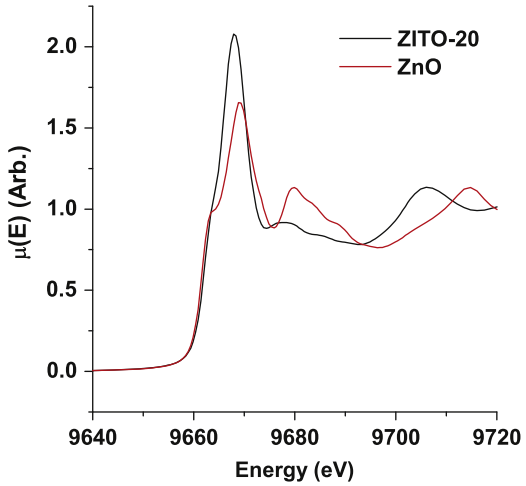

Fig. 11. (Color online) The near-edge regime of the normalized $\mu(E)$ of ZITO-20 and ZnO at the Zn K edge. The "white line" is the sharp feature located between 9665–9675 eV.

suggests that Zn is a neighbor to the In, Sn and Zn absorbers and the percentage of Zn neighboring the absorber is reflected by the total composition. This model is consistent with random substitutions of Zn and Sn for In with no detectable clustering. It should be noted that EXAFS measures the average local structure of the cations. Small regions of clusters and deviations from the nominal composition cannot be detected. As previously mentioned the bixbyite structure has two crystallographic cation positions, the b and d sites. Substituent order, symmetry-lowering and site preference of Zn and Sn is not evident by XRD or EXAFS owing to similar coordination environments of the b and d sites. Therefore, this structural model assumed neither Zn nor Sn substituted in In_2O_3 with a preference for the b or d site. The average local structure of ZITO shows good agreement with the model described by Zn and Sn-substituted-bixbyite In_2O_3 with no site preference.

5. Conclusion

EXAFS has been used to probe the local coordination environment of Zn, Sn and In to reveal significant features, and how they change, along the solid solution. The Zn and Sn reside at the bixbyite b and d sites, but their local coordination environments compared to In experience shorter distances for the first shell of six O, owing to the small cationic radii. These smaller octahedral units have the net effect on the structure to contract the lattice and to decrease the second nearest neighbor cation–cation distances as the amount of substitutional Zn and Sn increase. These EXAFS spectra are consistent with random substitutions of In by Zn and Sn, although clusters and small regimes of order would not be detected. Proffit et al [28] recently reported a crystalline ZITO thin film with the composition $In_{1.56}Sn_{0.24}Zn_{0.20}O_{3-\delta}$ and conductivity 1565 S/cm. As in this study, the EXAFS revealed Zn and Sn substitution of the In_2O_3 b and d sites. Both bulk and thin film ZITO demonstrate enhanced Zn and Sn solubility owing to the substitutional nature of the Zn and Sn leading to modestly reduced conductivities compared to ITO, but lowered In levels.

Acknowledgments

CAH was funded through the Materials Research Science and Engineering Center at Northwestern University supported by the National Science Foundation under NSF Award Number DMR-0520513. This work was performed at the Du-Pont-Northwestern-Dow Collaborative Access Team (DND-CAT) located at Sector 5 of the Advanced Photon Source (APS). DND-CAT is supported by E.I. DuPont de Nemours & Co., The Dow Chemical Company and the State of Illinois. Use of the APS was supported by the US Department of Energy, Office of Science, Office of Basic Energy Sciences, under Contract No. DE-AC02-06CH11357. The authors would like to thank Dr. Qing Ma for assistance with the EXAFS measurements and helpful discussions. This work made use of the J.B. Cohen X-ray Facility supported by the MRSEC program of the National Science Foundation (DMR-0520513) at the Materials Research Center of Northwestern University. The authors acknowledge T.O. Mason and D.E. Proffit for helpful discussions.

Appendix A. Supplementary materials

Supplementary data associated with this article can be found in the online version at doi:10.1016/j.jssc.2010.01.014.

References

[1] P.P. Edwards, A. Porch, M.O. Jones, D.V. Morgan, R.M. Perks, Dalton Trans. (2004) 2995.
[2] E. Fortunato, D. Ginley, H. Hosono, D.C. Paine, MRS Bull. 32 (2007) 242.
[3] G. Frank, E. Kauer, H. Kostlin, Thin Solid Films 77 (1981) 107.
[4] P. Nath, R.F. Bunshah, B.M. Basol, O.M. Staffsud, Thin Solid Films 72 (1980) 463.
[5] G.B. Palmer, K.R. Poeppelmeier, T.O. Mason, Chem. Mater. 9 (1997) 3121.
[6] S.P. Harvey, T.O. Mason, D.B. Buchholz, R.P.H. Change, C. Korber, A. Klein, J. Am. Ceram. Soc. 91 (2008) 467.
[7] M. Marezio, Acta Crystallogr. 20 (1966) 723.
[8] S.P. Harvey, K.R. Poeppelmeier, T.O. Mason, J. Am. Ceram. Soc. 91 (2008) 3683.
[9] T.O. Mason, G.B. Gonzalez, J.-H. Hwang, D.R. Kammler, Phys. Chem. Chem. Phys. 5 (2003) 2183.
[10] M. Newville, P. Livins, Y. Yacoby, J.J. Rehr, E.A. Stern, Jpn. J. Appl. Phys. Part I 32 (1993) 125.
[11] B. Ravel, M. Newville, J.O. Cross, C.E. Bouldin, Physica B 209 (1995) 145.
[12] B. Ravel, M. Newville, J. Synchrotron Radiat. 12 (2005) 537.
[13] M. Newville, J. Synchrotron Radiat. 8 (2001) 322.
[14] M. Newville, J. Synchrotron Radiat. 8 (2001) 96.
[15] J.J. Rehr, S.I. Zabinsk, FEFF5: An ab Initio Multiple Scattering XAFS Code, Seattle, WA, Department of Physics, University of Washington, 1992, p. 5.
[16] S.D. Kelly, D. Hesterberg, B. Ravel, in: A.L. Ulery, L.R. Drees (Eds.), Methods of Soil Analysis. Part 5. Mineralogical Methods, Vol. 5, Soil Society of America, Inc., Madison, 2008.
[17] R.D. Shannon, Acta Crystallogr. A 32 (1976) 751.
[18] L. Vegard, Z. Phys. 5 (1921) 17.
[19] W.H. Baur, A.A. Khan, Acta Crystallogr. B 27 (1971) 2133.
[20] T.M. Sabine, S. Hogg, Acta Crystallogr. B 25 (1969) 2254.
[21] G.B. Gonzalez, T.O. Mason, J.P. Quintana, O. Warschkow, D.E. Ellis, J.-H. Hwang, J.P. Hodges, J.D. Jorgensen, J. Appl. Phys. 96 (2004) 3912.
[22] N. Nadaud, N. Lequeux, M. Nanot, J. Jove, T. Roisnel, J. Solid State Chem. 135 (1998) 140.

[23] P. Parent, H. Dexpert, G. Tourillon, J.-M. Grimal, J. Electrochem. Soc. 139 (1992) 276.
[24] P. Parent, H. Dexpert, G. Tourillon, J.-M. Grimal, J. Electrochem. Soc. 139 (1992) 282.
[25] G.A. Waychunas, C.C. Fuller, J.A. Davix, J.J. Rehr, Geochim. Cosmochim. Acta 67 (2003) 1031.
[28] D.E. Proffit, D.B. Buchholz, R.P.H. Chang, M.J. Bedzyk, T.O. Mason, Q. Ma, J. Appl. Phys. 106 (2009) 113524.